IEEE Access
Multidisciplinary | Rapid Review | Open Access Journal

Received July 11, 2021, accepted August 8, 2021, date of publication August 12, 2021, date of current version August 19, 2021.

Digital Object Identifier 10.1109/ACCESS.2021.3104302

Satellite Remote Sensing Image Stereoscopic Positioning Accuracy Promotion Based on Joint Block Adjustment With ICESat-2 Laser Altimetry Data

XINLEI ZHANG, SHUAI XING, QING XU, GUOPING ZHANG, PENGCHENG LI, AND KUN CHEN
The Institute of Geospatial Information, Strategic Support Force Information Engineering University, Zhengzhou 450001, China

Corresponding authors: Xinlei Zhang (zxl9602@163.com) and Shuai Xing (xing972403@163.com)

This work was supported by the National Natural Science Foundation of China under Grant 41876105 and Grant 41371436.

ABSTRACT The next generation Ice, Cloud, and Land Elevation Satellite-2 (ICESat-2)/Advanced Topographic Laser Altimeter System (ATLAS) was launched in 2018 to provide large amounts of spaceborne laser altimetry data. The joint block adjustment with laser altimetry data and satellite remote sensing images can promote limited stereoscopic positioning accuracy without ground control points (GCPs). However, there are two problems in the joint block adjustment, that is, the reliable ATLAS laser altimetry points (LAPs) selection and the discrepancies of image-object points. To solve the above problems, a surface point cloud extraction algorithm based on wavelet reconstruction was proposed. Then, the LAPs selection constraint model was established, so the terrain influence was resolved. Finally, a block joint adjustment method has been proposed with remote sensing images and the reliable LAPs considering error of their plane coordinates, which could achieve the accurate corresponding image points of the reliable LAPs, remarkably decrease the discrepancies of image-object points. Fourteen pairs of ATLAS data, seven ZY3-02 stereo images and eleven Mapping Satellite-1 stereo images in Zhengzhou, China were collected to validate the method performance. Experiment results have shown that the consistency of the image-object points and the positioning accuracy of stereoscopic images without GCPs have been improved. Compared with the free net block adjustment, the height, east and north positioning accuracy of ZY3-02 and Mapping Satellite-1 stereo images have increased by 61%, 56%, 60% and 56%, 38%, 37%, respectively.

INDEX TERMS Joint block adjustment, laser altimeter, ICESat-2, ZY3-02 satellite, mapping satellite-1, stereo images.

I. INTRODUCTION

Remote sensing satellites provide high-quality surveying and mapping products. High-precision stereo surveying typically uses uniform GCPs to ensure accurate geometric positioning of satellite image block adjustment. However, obtaining high-precision data from GCPs is time consuming and labor intensive, and in some areas, it is difficult to obtain ground control information, which makes it challenging to further improve the accuracy of stereo mapping.

With the continuous development of laser technology, satellite laser height measurement capability is getting stronger and stronger. Higher precision and denser laser altimeter data can be obtained, which can improve the accuracy of stereo mapping without GCPs. Much of the work on the combined processing of optical camera images and laser altimeter data began on planetary observations. In the applications of Mars topographic mapping, Rosiek *et al.* [1] used Mars Orbiter Laser Altimeter (MOLA) laser ranging information as the control information for Viking Orbiter images to perform bundle adjustment. After image matching and automatic digital elevation model (DEM) extraction, a 1:500,000 scale Mars mapping product was produced. Yoon and Shan [2] proposed a joint processing method for Mars Orbiter Camera imagery and MOLA to correct misregistration. In the applications of lunar topographic mapping,

The associate editor coordinating the review of this manuscript and approving it for publication was Yongqiang Zhao.

Di *et al.* [3] proposed cross-point adjustment and sensor model refinement to co-register Chang'E-1 stereo images and laser altimetry data. He *et al.* [4] researched a laser altimeter data assisted block adjustment method using a rational function model (RFM). All these studies suggest that the combined processing of planetary laser altimetry data and optical images can effectively improve the accuracy of planetary surface topography mapping.

For Earth observations, the Geoscience Laser Altimeter System (GLAS) laser altimeter launched on the United States Ice, Cloud, and Land Elevation Satellite (ICESat) is the first Light Detection and Ranging (LiDAR) system used for Earth observations to obtain voluminous high-precision elevation data. For reliable LAPs selection, Duong *et al.* [5] used the three parameters of saturation correction flag, gain value and elevation use flag to eliminate gross errors in GLAS laser height measurement data. Wang *et al.* [6] used echo waveform width, crest number, skewness, kurtosis and reflectivity to filter GLAS. Li *et al.* [7] used a method based on random forests to extract satellite laser altimetry footprints that meet the elevation accuracy requirements of certain applications in complex terrain.

For LAPs and stereo images joint block adjustment, Li *et al.* [8] added GLAS data to the block adjustment of the ZY3-01 satellite, improving the height accuracy to 3 m without GCPs. Li *et al.* [9], [10] verified that using joint adjustment in generating the digital surface model (DSM) was better than the direct correction DSM. Wang *et al.* [11] proposed an ICESat laser point-assisted block adjustment method for stereo satellite images to improve the positional accuracy of Mapping Satellite-1 imagery without GCPs. When using 1839 ICESat elevation control points automatically extracted from the survey area to assist the block adjustment, the height accuracy can be increased to 2.51 m. Cao *et al.* [12] proposed a geometric imaging model of the refinement of satellite stereo images aided with laser altimeter data. The experiments in ZY3-02 indicated that the height accuracy of the satellite geometry model refined using the laser altimeter data reached 3.23 m. Above previous studies showed that the height accuracy can be greatly improved without adding GCPs. However, GLAS laser footprints are too sparse to make further analysis.

The next generation of the LiDAR satellite ICESat-2 was launched in 2018. The onboard LiDAR altimetry system ATLAS is a micro-pulse photon-counting LiDAR system [13]. Multi-beam LiDAR is the latest laser detection technology, which has a high laser spot measurement accuracy, large surveying bandwidth, small spot area, high repetition frequency, and high resolution [14], [15]. ICESat-2 is the first photon-counting Earth observation system, whose 10 kHz repetition frequency makes the foot spacing along the track 70 cm and its foot diameter 17 m (GLAS is 40 Hz, 170 m, 70 m, respectively) [16]. In addition, it employs six beams arranged in three pairs where each group has a strong beam and a weak beam. This design can increase the density of altimetry points.

ATLAS can be used to measure surface elevation, including the elevation of ice sheets, forests, and oceans, and to provide a reliable basis for topographic scientific research and for monitoring global climate change trends based on biomass. So, it can provide high-precision laser footprints on the global land surface [17], [18] and high-precision control data for the stereoscopic positioning of satellite stereo images. Wang *et al.* [19] studied the extraction of global elevation control points based on elevation reference and ATL08 attribute parameters. However, ATL08 product contains data categorized as land at 100-meter intervals, which scale range is too large to reliable LAPs selection. What is worse, there was no research on the use of ICESat-2 LAPs for joint block adjustment. The key problem is that the exact location of LAPs cannot be determined, so it is difficult to guarantee the consistency of the object-image points.

In this study, we present a joint block adjustment method for spaceborne laser altimetry data and satellite stereo images. Different from previous work, this study proposes (1) a multi-constraint filter to select reliable ATLAS LAPs; (2) an iterative plane coordinate correction of the selected ATLAS LAPs during the joint block adjustment. Stereo images and laser altimeter data covering the research areas in Zhengzhou, China were collected to conduct experiments, and several types of adjustment plans were designed to discuss their influence on the block adjustment results.

II. MATERIALS

A. EXPERIMENTAL AREA

The experimental site in Zhengzhou in Central China were selected. The relevant information about the study area, is shown in Figure 1. The terrain is generally high in the southwest and low in the northeast, showing a stepwise decline. The survey area included mountains, hills, and plains with a height difference of more than 1400 m.

B. ICESat-2 DATA

ATLAS provides a total of 22 data products (ATL01–ATL21). Land-related data products include ATL03, ATL08, and ATL18 [20]. ATL03, the global geolocated photon product, includes time, latitude, longitude, and height information of each photon event [21]. ATL03 products have higher spatial resolution than ATL08 and ATL18.From October 25, 2018 to October 29, 2019, fourteen pairs of ATL03 datasets were selected to cover the entire test area, as shown in Figure 1.

C. IMAGE DATA

ZY3-02 stereo images and the Mapping Satellite-1 stereo images were collected. ZY3-02 satellite, which was launched on May 30, 2016, is the second satellite in the ZiYuan3 series and mainly used for developing the civil space infrastructure in China. For satellite ZY3-02, the ground sample distance (GSD) for forward-view (FWD) and backward-view (BWD) imagery is 2.5 m, whereas for nadir-view (NAD) imagery, it is 2.1 m [22]. Seven ZY3-02 three-line-array stereo images were acquired from March 13, 2019 to July 3, 2019.

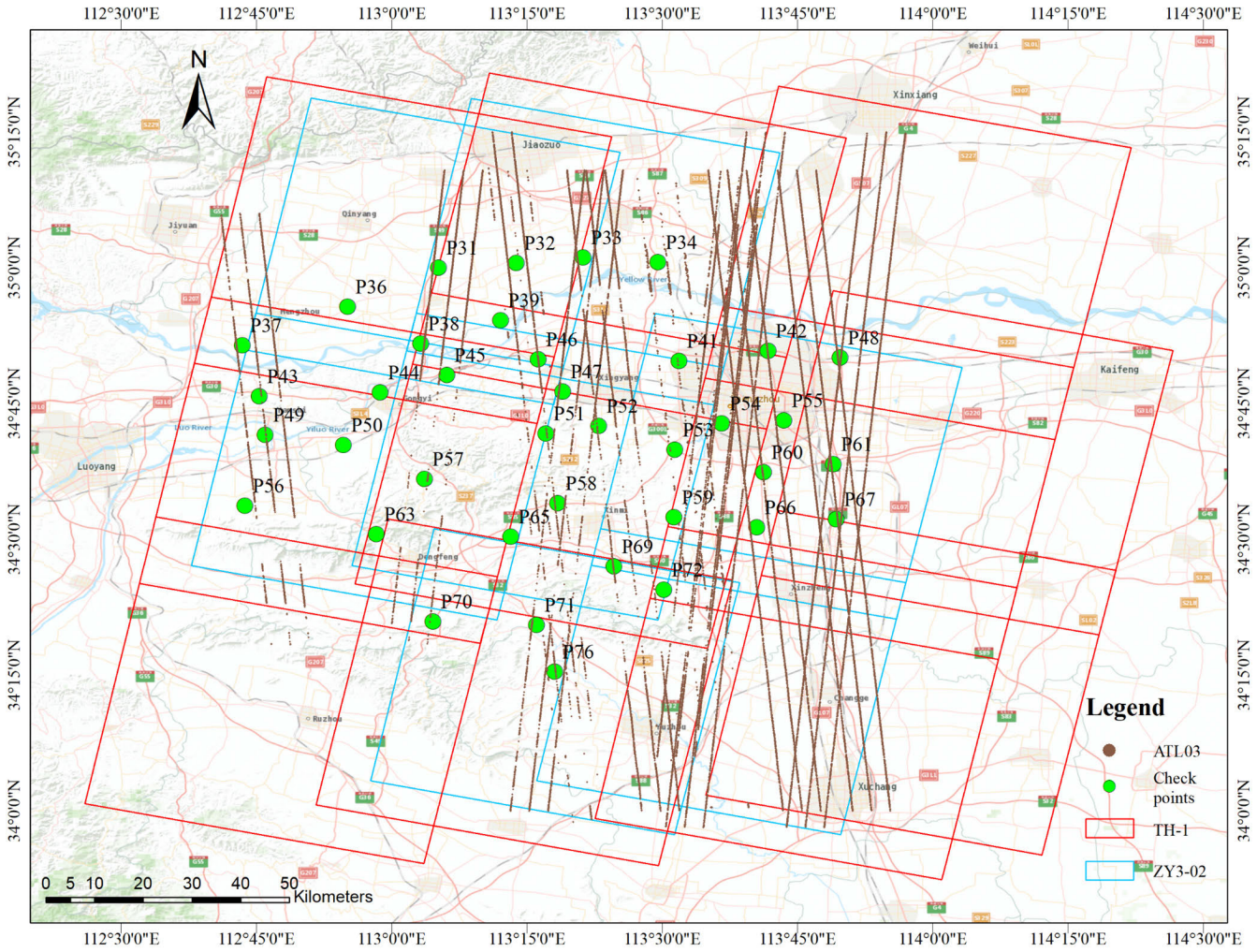

FIGURE 1. Experimental data and reference data.

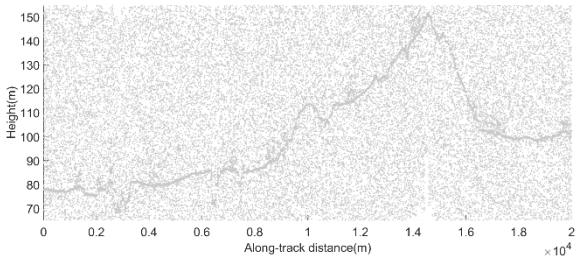

FIGURE 2. ATL03 raw point cloud distribution.

The Mapping Satellite-1 is the first stereo mapping satellite in China. Three satellites of Mapping Satellite-1 were launched on August 24, 2010, May 6, 2012, and October 26, 2015, respectively. For Mapping Satellite-1, all GSDs are 5 m [23]. Eleven Mapping Satellite-1 three-line-array stereo images were acquired from September 25, 2019 to April 27, 2020.

D. CHECK DATA

We collected 38 high-accuracy check points (CPs) to validate the results. The CPs were surveyed using the Real-Time Kinematic Global Positioning System (RTK-GPS), which ensures that the geolocation accuracy of the CPs is better than 0.1 m. The CPs distribution is shown in Figure 1.

Unmanned aerial vehicle (UAV) LiDAR data, considered as a reference dataset, were collected. The absolute height accuracy of the UAV LiDAR data was better than 0.15 m. Publicly available 12.5-m DEM data, i.e., the Advanced Land Observing Satellite (ALOS) satellite phased array L-band synthetic aperture radar (PALSAR) high-resolution terrain corrected product, was collected for slope calculation and accuracy evaluation.

III. METHODS

To select the reliable LAPs, the principle of MODWT was introduced, then it was applied to extract LAPs with other multiple constraints. The basic principle of joint block adjustment was introduced later. Aiming at the problem of errors in LAPs plane coordinates and no accurate image points, an optimized adjustment scheme considering the plane coordinate error of the LAPs was proposed.

A. RELIABLE LAPs SELECTION

1) MODWT BASED ON THE OTSU METHOD

Figure 2 shows a section of the ATL03 point cloud data. There are many randomly distributed noise points. Although signal points are denser than noise points, it is difficult to distinguish ground points from raw data due to the large amount of noise. The distribution of ground points changes with topography, which shows continuous and smooth low-frequency signal characteristics. Thus, raw point cloud data can be treated as a set of discrete digital signals. Therefore, digital signal processing methods can be used to extract the ground points.

Maximum overlap discrete wavelet transform (MODWT) has the translation invariance of wavelet coefficients and scale coefficients, and all the decomposition layers retain the same time resolution without phase distortion [24]. The signal length does not decrease after decomposition, and it has a good decomposition and reduction effect. The adaptive threshold determination avoids errors that may be caused by the traditional method of setting the threshold in advance. In multi-resolution analysis, a signal can be approximated at progressively coarser scales while recording the differences between approximations at consecutive scales.

The MODWT can be expressed as a linear combination of the scaling function $\varphi(x)$ and wavelet $\psi(x)$ at varying scales and translations.

$$f(x) = \sum_{k=0}^{N-1} c_k 2^{-J_0/2} \varphi\left(2^{-J_0}x - k\right) + \sum_{j=1^{J_0}} \sum_{k=0}^{N-1} d_{j,k} 2^{j/2} \psi\left(2^{-j}x - k\right) \quad (1)$$

where J_0 is the number of wavelet decomposition levels. The first sum is the coarse-scale approximation of the signal, and the second sum is the details at successive scales. The MODWT returns N coefficients c_k and ($J_0 \times N$) detail coefficients $d_{j,k}$ of the expansion.

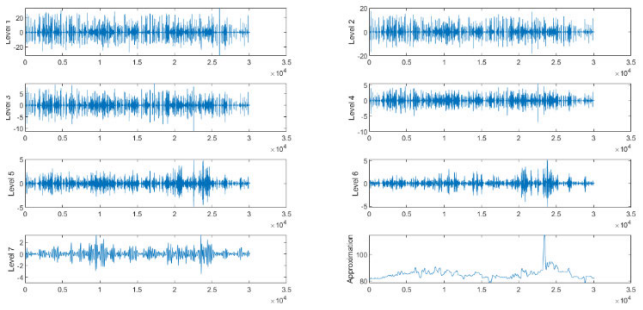

FIGURE 3. Wavelet decomposition result.

Figure 3 shows wavelet decomposition results of 2019.04.05 23:38:41 gt1l track for $f(x)$, each level of wavelet components and redundant items. With an increase in the decomposition order, the frequency of wavelet components continues to decrease, the signal change trend is more stable and obvious in the low-frequency component, and the noise in the original data is concentrated in the high-frequency part, i.e., the low-order component. The most stable low-frequency signal can be separated from the original data by removing the high-frequency wavelet components and reconstructing the signal [25].

To extract the ground points from the raw point cloud, high-frequency and low-frequency wavelet components of the raw point cloud was obtained through the MODWT algorithm. Then, high-frequency components were removed by setting the cutoff frequency, and the point cloud was reconstructed. Finally, based on the assumption of continuous changes in terrain undulations, the height difference between the reconstructed point cloud and the raw point cloud was calculated, and the points whose height difference was less than a certain threshold were marked as ground points.

To maximize the distinction between signal and noise, the Otsu method was used to calculate the cutoff frequency, and the photons were adaptively divided into signal and noise [26]. The level threshold ($\boldsymbol{x}$) was calculated using the Otsu method as follows:

$$\begin{cases} \omega_0(t) = \dfrac{t}{n} \\ \omega_1(t) = 1 - \dfrac{t}{n} \\ \mu_0(t) = \dfrac{\sum_{i=1}^{t} x(i)}{t} \\ \mu_1(t) = \dfrac{\sum_{i=t+1}^{n} x(i)}{n-t} \\ \mu(t) = \omega_0(t)\,\mu_0(t) + \omega_1(t)\,\mu_1(t) \\ \sigma^2 = \omega_0(t)\,(\mu_0(t) - \mu(t))^2 + \omega_1(t)\,(\mu_1(t) - \mu(t))^2 \end{cases} \quad (2)$$

where $\boldsymbol{n}$ is the total number of photons and $\boldsymbol{t}$ is the number of photons currently assumed to be the signal.

When the inter-class variance σ^2 is largest, the sum of the low-frequency wavelet components and redundant terms can best represent the height distribution of the ground points.

2) LAPs SELECTION WITH MULTIPLE CONSTRAINTS

Although photon-counting LiDAR has the advantages of low energy consumption, high measurement sensitivity, and high repetition frequency, it also entails new problems. The adoption of green wavelength lasers (532 nm) and high detection sensitivity make it susceptible to the influence of atmospheric scattering noise and solar background noise [27], [28]. In addition, ATLAS laser altimetry data do not have synchronized observation images; thus, it is impossible to strictly determine the exact ground position of the photon. Moreover, different topography and atmospheric conditions have a greater impact on the measurement accuracy of the photon geographic coordinates. Therefore, it is necessary to select reliable points from laser altimetry data as GCPs.

The ground curve can be extracted using the identification parameters recorded in the ATL03 and ATL08 data [29]. Although the extraction result is satisfactory, prior identification indicators should be used in the ATL product. To solve the problem in which the raw photon-counting laser altimetry data independently extract the surface curve and control

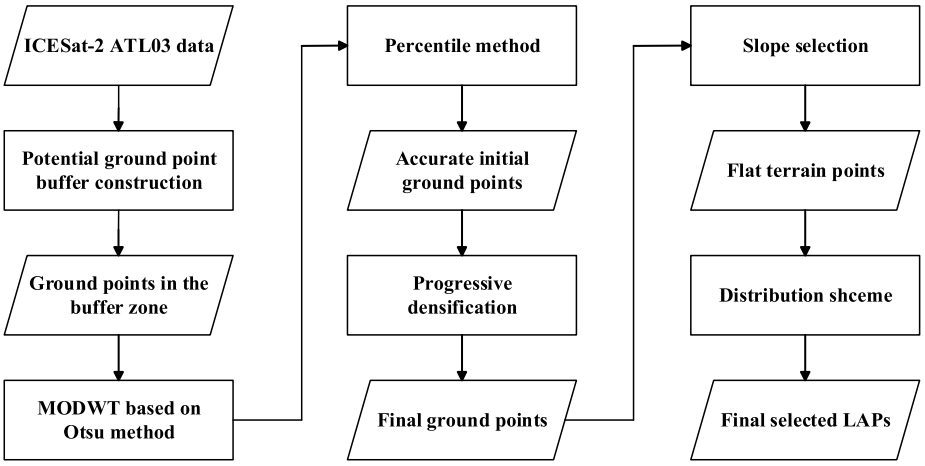

FIGURE 4. Flow chart of reliable LAPs selection method.

points without evaluation parameters, the control point selection method is designed as shown in Figure 4.

(1) Potential ground point buffer construction

To reduce redundant calculations and eliminate obvious ATL03 noise points, a buffer containing all potential ground points was created, and an elevation frequency histogram was used to remove obvious noise points in the data for each buffer [30].

(2) Modwt initial ground points extraction

Since there is no unified standard for the selection of the wavelet basis function, in this study, the sym7 wavelet basis function was selected based on the denoising experience [31], [32]. Because it integrates compact support, orthogonality, and symmetry, the sym7 wavelet basis function has time-frequency characteristics that can effectively separate the random error and useful information in the signal and obtain a better smoothing effect when reconstructing the signal.

Through MODWT based on the Otsu method, the point cloud was reconstructed after removing high-frequency components, and the points with small height changes were retained. Because there was always a small number of noise points distributed around the ground points, with similar frequency characteristics to the ground points, the ground points extracted by MODWT using the Otsu method were still mixed with a small amount of misclassified point clouds.

(3) Misclassified points removal using the percentile method To ensure the reliability of the initial ground points, the percentile method was used to further filter the MODWT extraction results. The percentile method is often used to extract unsteady time-frequency analysis data and has a strong adaptive ability to data changes. It first arranges the data within a certain range in ascending order, then calculates the cumulative percentage corresponding to each data point, and finally outputs the value of the data point corresponding to a certain percentage as required.

To remove the interference of misclassified points around the ground point, a 20-m window was used to traverse along the track to optimize the ground points extracted by MODWT. The point cloud height in the window was calculated, and only the ground points within the height range of [15%, 25%] were maintained. The window width value was based on the recommendation of the ICESat-2 science team [33]; a 20-m window can better maintain surface details when accurate ground points are extracted, whereas a larger window will cause the ground surface to be too smooth, with ground points distributed in steps, while a smaller window will significantly reduce the calculation efficiency. A larger quantile range will mistakenly extract non-ground points, whereas a smaller range will result in vacancies in the ground points of some windows. Thus, [15%, 25%] was used as the quantile range for ground point selection to ensure the reliability of the extraction results.

(4) Progressive densification

Because the number of accurate ground points was not sufficient to restore the ground curve, it was necessary to use the triangular irregular network densification algorithm to select more ground points from the original data. In the encryption process, the distance from the point to the current ground curve was considered, and the distance threshold was set to 1 m. Accurate ground points were connected in chronological order, and the point whose distance was less than the threshold was selected as the new ground point from the point set divided by any two accurate ground points. This step was repeated until the number of ground points no longer increased.

(5) Final laps selection

After the final ground points were extracted, the maximum slope value in each direction of the plane position where the final ground point is located was calculated using DEM data. The final ground points with a maximum slope of less than 6° and no significant change in the slope within 20 m of the neighborhood were selected as flat terrain points.

Finally, to ensure that the final LAPs have a uniform distribution, they should be selected as uniformly as possible according to the image arrangement relationship.

B. JOINT BLOCK ADJUSTMENT OF SATELLITE STEREO IMAGES AND LASER ALTIMETRY DATA

1) BLOCK ADJUSTMENT BASED ON RATIONAL FUNCTION MODEL

The RFM is a general sensor model suitable for various sensors and commonly used for high-resolution optical satellite sensors [34]. RFM considers the object-space coordinates as the independent variables and the image-space coordinates as the dependent variables:

$$\begin{cases} r_n = \dfrac{Num_S(X_n, Y_n, Z_n)}{Den_S(X_n, Y_n, Z_n)} = \dfrac{\sum_{i=0}^{3}\sum_{j=0}^{3}\sum_{k=0}^{3} p_1^{ijk} X_n^i Y_n^j Z_n^k}{\sum_{i=0}^{3}\sum_{j=0}^{3}\sum_{k=0}^{3} p_2^{ijk} X_n^i Y_n^j Z_n^k} \\ c_n = \dfrac{Num_L(X_n, Y_n, Z_n)}{Den_L(X_n, Y_n, Z_n)} = \dfrac{\sum_{i=0}^{3}\sum_{j=0}^{3}\sum_{k=0}^{3} p_3^{ijk} X_n^i Y_n^j Z_n^k}{\sum_{i=0}^{3}\sum_{j=0}^{3}\sum_{k=0}^{3} p_4^{ijk} X_n^i Y_n^j Z_n^k} \end{cases} \tag{3}$$

where (c_n, r_n) and (X_n, Y_n, Z_n) are the normalized image-space coordinates and corresponding object-space coordinates, respectively, and $p_n^{ijk}(n = 1, 2, 3, 4)$ are the polynomial coefficients.

The normalized coordinates can be expressed as in (4):

$$\begin{cases} c_n = \dfrac{c - c_0}{c_s}, \quad r_n = \dfrac{r - r_0}{r_s} \\ X_n = \dfrac{X - X_0}{X_s}, \quad Y_n = \dfrac{Y - Y_0}{Y_s}, \; Z_n = \dfrac{Z - Z_0}{Z_s} \end{cases} \tag{4}$$

where (c, r) and (X, Y, Z) are the image-space coordinates and corresponding object-space coordinates, respectively; c_0, r_0, X_0, Y_0, Z_0 are the offset parameters, and c_s, r_s, X_s, Y_s, Z_s are the scale parameters.

The RFM-compensated model can be expressed as in (5) [35]:

$$\begin{cases} c = c_s \cdot \dfrac{Num_S(X_n, Y_n, Z_n)}{Den_S(X_n, Y_n, Z_n)} + c_0 + \Delta c \\ r = r_s \cdot \dfrac{Num_L(X_n, Y_n, Z_n)}{Den_L(X_n, Y_n, Z_n)} + r_0 + \Delta r \end{cases} \tag{5}$$

where $(\Delta c, \Delta r)$ are the compensated values for the image-space coordinates.

$$\begin{cases} \Delta c = a_0 + a_1 c + a_2 r \\ \Delta r = b_0 + b_1 c + b_2 r \end{cases} \tag{6}$$

where $a_i, b_i\,(i = 0, 1, 2)$ are the affine transformation coefficients.

The least-squares form of the RFM-compensated equations can be represented in the matrix form as follows:

$$\begin{pmatrix} v_{c_{ij}} \\ v_{r_{ij}} \end{pmatrix} = \begin{pmatrix} \frac{\partial c_{ij}}{\partial a_{oj}} & \frac{\partial c_{ij}}{\partial a_{1j}} & \frac{\partial c_{ij}}{\partial a_{2j}} & 0 & 0 & 0 \\ 0 & 0 & 0 & \frac{\partial r_{ij}}{\partial b_{oj}} & \frac{\partial r_{ij}}{\partial b_{1j}} & \frac{\partial r_{ij}}{\partial b_{2j}} \end{pmatrix} \begin{pmatrix} da_{oj} \\ da_{1j} \\ da_{2j} \\ db_{oj} \\ db_{1j} \\ db_{2j} \end{pmatrix}$$

$$+ \begin{pmatrix} \frac{\partial c_{ij}}{\partial X_i} & \frac{\partial c_{ij}}{\partial Y_i} & \frac{\partial c_{ij}}{\partial Z_i} \\ \frac{\partial r_{ij}}{\partial X_i} & \frac{\partial r_{ij}}{\partial Y_i} & \frac{\partial r_{ij}}{\partial Z_i} \end{pmatrix} \begin{pmatrix} dX_i \\ dY_i \\ dZ_i \end{pmatrix} - \begin{pmatrix} c_{ij} - \bar{c}_{ij} \\ r_{ij} - \bar{r}_{ij} \end{pmatrix} \begin{pmatrix} p_{c_{ij}} \\ p_{r_{ij}} \end{pmatrix} \tag{7}$$

The matrix form is expressed as in (8):

$$\boldsymbol{V} = \boldsymbol{A}\,\boldsymbol{t} + \boldsymbol{B}\,\boldsymbol{x} - \boldsymbol{l}\,\boldsymbol{P} \tag{8}$$

where $\boldsymbol{V}$ is the residual vector for the RFM-compensated equations, $\boldsymbol{A}$ and $\boldsymbol{B}$ are the observation matrices for the RFM-compensated equations, $\boldsymbol{t}$ is the vector of the affine transformation coefficient correction numbers, $\boldsymbol{x}$ is the vector of coordinate correction numbers connected to the object side, $\boldsymbol{l}$ is the approximation vector, and $\boldsymbol{P}$ is the weight matrix.

2) JOINT BLOCK ADJUSTMENT

It is difficult to use LAPs directly as control points. On the one hand, it is not clear about their exact position on the ground. The plane and height accuracy of LAPs are better than 5m and 0.3m respectively [14], [15]. The height error is acceptable, while the plane error has an impact on the adjustment result. On the other hand, the coordinates of the image points directly calculated by RPC are not accurate. Due to errors in the original RPC parameters of images, for the same LAP overlaid on the NAD, BWD, FWD images, the image points on three-view images are not the homologous points.

Without GCPs, the parameters to be adjusted as free unknowns will cause the adjustment accuracy to be unstable, and system errors will continue to accumulate. To improve the overall adjustment accuracy of the satellite stereo images, the basic process of the joint block adjustment with LAPs and satellite stereo images is described as follows. First, the geometric models of the satellite stereo images were built in the survey area, and the tie points of the stereo images were obtained by image registration. Then, free network adjustment without constraints was used to obtain a high-precision relative accuracy. The ground coordinates of the tie points were calculated using the original rational polynomial coefficients (RPC) of the image and the affine transformation correction parameters to execute space intersection with multiple images. For the selected LAPs $P(X, Y, Z)$, the corresponding image coordinates were obtained by the RPC normal solution. By using the LAPs projected on the NAD image point p_i as references, the LAPs on the BWD and FWD images were obtained by image matching. Finally, tie points and LAPs were jointly used in the adjustment. This is recorded as a scheme that does not consider the plane coordinate error of the LAPs.

While the plane coordinate has an error, it is difficult to satisfy the consistency of the image-object points. To improve the consistency of the image-object points of the LAPs and reduce the error of the object-plane coordinates, it is necessary to adopt an optimization strategy during the adjustment process. The workflow is shown in Figure 5.

The NAD image point p_i of the LAPs was acquired, and the corresponding ground points $P_I(X_1, Y_1, Z_1)$ were calculated through space intersection with multiple images. The initial

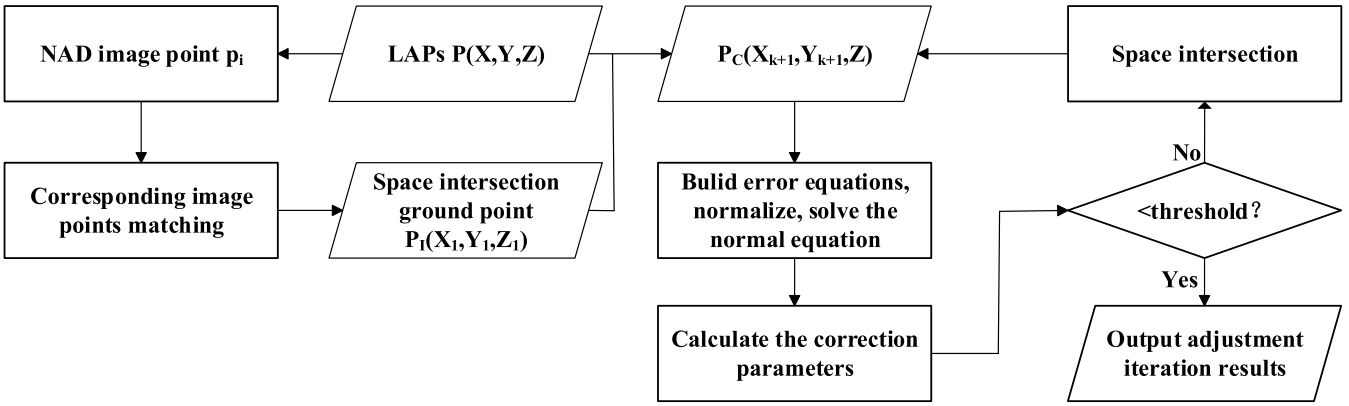

FIGURE 5. Flow chart of joint block adjustment optimization method.

value P_C was set as (X_1, Y_1, Z). The LAPs were joined into the adjustment model as control points with errors in the plane coordinates. The error equation was constructed according to (9): The weight of the error equation of the control points was set multiple orders of magnitude higher than those of the tie points, and the height value Z of point P_C was taken as the true value.

Through the above steps, the error equation was normalized and solved. In the kth iteration, the affine transformation coefficient and the ground coordinates of tie points were calculated by the least-squares method. Thus, the plane coordinates of LAPs were updated after every iteration. The iteration ended until the residuals of the $\boldsymbol{P_C}$ plane coordinate met the threshold.

This scheme was recorded considering the plane coordinate error of the LAPs. The optimization scheme makes the object-space coordinate closer to the true values by continuously iterating the plane coordinates of the LAPs, improving the consistency of image-object points, and the plane accuracy of the LAPs.

$$\begin{pmatrix} v_{c_{ij}} \\ v_{r_{ij}} \end{pmatrix} = \begin{pmatrix} \frac{\partial c_{ij}}{\partial a_{oj}} & \frac{\partial c_{ij}}{\partial a_{1j}} & \frac{\partial c_{ij}}{\partial a_{2j}} & 0 & 0 & 0 \\ 0 & 0 & 0 & \frac{\partial r_{ij}}{\partial b_{oj}} & \frac{\partial r_{ij}}{\partial b_{1j}} & \frac{\partial r_{ij}}{\partial b_{2j}} \end{pmatrix} \begin{pmatrix} da_{oj} \\ da_{1j} \\ da_{2j} \\ db_{oj} \\ db_{1j} \\ db_{2j} \end{pmatrix} + \begin{pmatrix} \frac{\partial c_{ij}}{\partial X_i} & \frac{\partial c_{ij}}{\partial Y_i} \\ \frac{\partial r_{ij}}{\partial X_i} & \frac{\partial r_{ij}}{\partial Y_i} \end{pmatrix} \begin{pmatrix} dX_i \\ dY_i \end{pmatrix} - \begin{pmatrix} c_{ij} - \bar{c}_{ij} \\ r_{ij} - \bar{r}_{ij} \end{pmatrix} \begin{pmatrix} p_{c_{ij}} \\ p_{r_{ij}} \end{pmatrix} \quad (9)$$

IV. RESULTS

A. SELECTION OF RELIABLE LAPs

To effectively execute block adjustment based on ATL03 LAPs and satellite stereo images, ATL03 ground points need to be extracted first. When extracting the ground points, the ground point sequence can be regarded as a trend signal

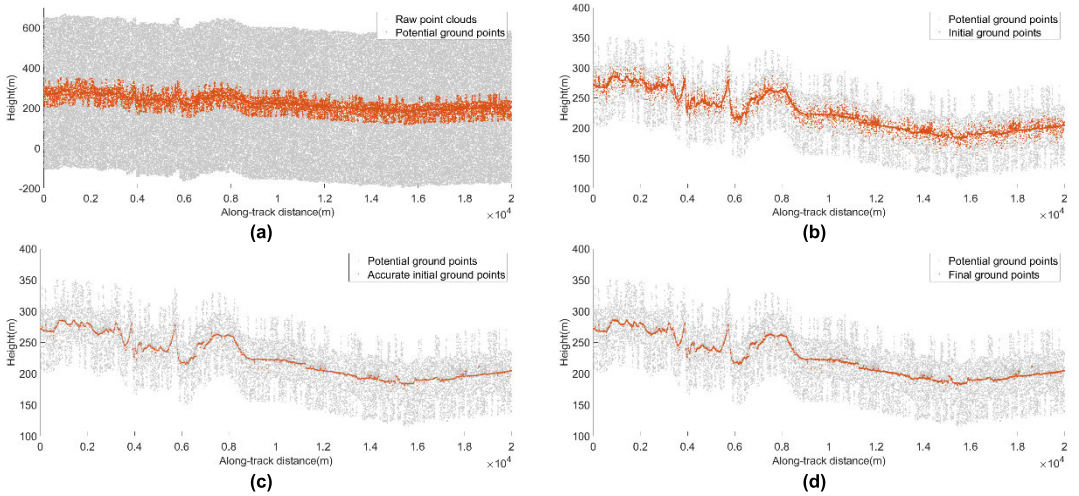

FIGURE 6. Each step of ground point extraction. (a) Ground point buffer creation, (b) MODWT extraction result, (c) percentile method extraction result, and (d) progressive densification extraction result.

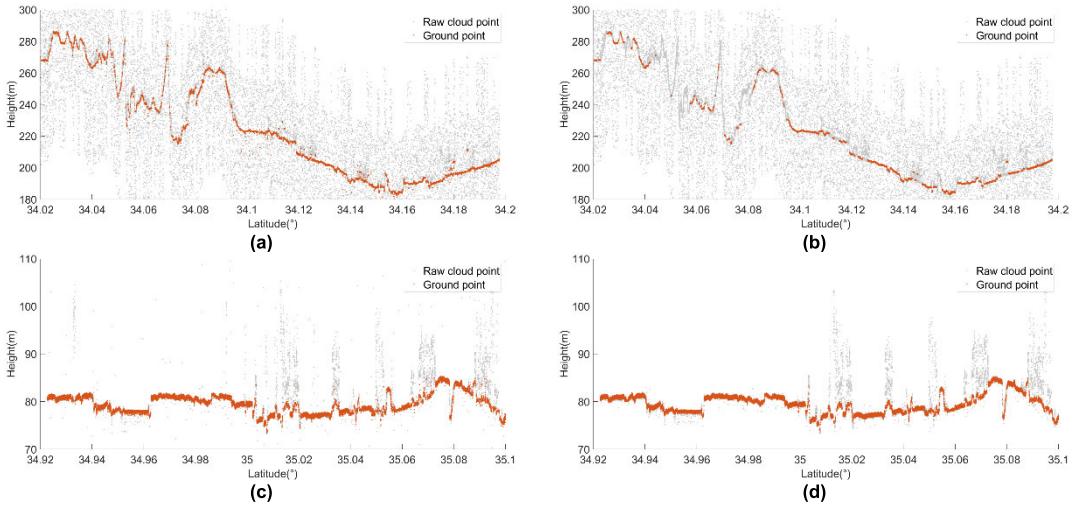

FIGURE 7. Comparison of ground point extraction. (a) MODWT extraction result 1, (b) extraction result 1 of [29], (c) MODWT extraction result 2, and (d) extraction result 2 of [29].

TABLE 1. Statistical results for RMSE and R^2 between selected LAPs and ALOS DEM.

Type	ATL03 Acquisition Time(UTC)	MODWT extraction		Extraction result of [29]	
		RMSE/m	R^2	RMSE/m	R^2
Day data	2018.10.25 19:27:29	2.545	0.9994	2.6	0.9989
	2018.11.23 18:03:32	2.556	0.9998	2.628	0.9979
	2018.12.26 16:31:14	2.495	0.9997	2.814	0.9996
	2019.02.22 13:43:29	2.319	0.9969	2.415	0.9959
	2019.03.23 12:19:30	2.356	0.9883	2.527	0.9810
	2019.06.02 20:50:35	1.872	0.9989	2.394	0.9985
	2019.09.30 15:06:30	2.286	0.9982	2.490	0.9980
	2019.10.29 13:42:34	2.131	0.9886	2.391	0.9860
Night Data	2019.01.01 04:07:09	2.749	0.9972	3.086	0.9945
	2019.03.04 01:11:01	2.302	0.9994	2.609	0.9988
	2019.04.01 23:47:00	1.940	0.9968	2.3332	0.9948
	2019.04.05 23:38:41	2.624	0.9997	3.257	0.9997
	2019.04.30 22.22.58	2.002	0.9843	2.131	0.9793
	2019.05.24 09:23:05	1.931	0.9929	2.157	0.9901

TABLE 2. ATL03 LAPs selection results.

Type	ATL03 Acquisition Time(UTC)	Original Points	After MODWT	Denoising Rejection Rate	After Slope Selection	Slope Rejection Rate
Day data	2018.10.25 19:27:29	950,024	246,343	74.07%	191,103	22.42%
	2018.11.23 18:03:32	187,890	46,162	75.43%	40,365	12.56%
	2018.12.26 16:31:14	357,756	102,845	71.25%	74,916	27.16%
	2019.02.22 13:43:29	137,563	31,600	77.03%	29,386	7.01%
	2019.03.23 12:19:30	683,812	262,752	61.58%	256,139	2.52%
	2019.06.02 20:50:35	300,353	98,227	67.30%	86,699	11.74%
	2019.09.30 15:06:30	95,963	18,074	81.17%	16,405	9.23%
	2019.10.29 13:42:34	606,291	204,787	66.22%	197,280	3.67%
Night Data	2019.01.01 04:07:09	2,153,938	91,907	95.73%	82,787	9.92%
	2019.03.04 01:11:01	2,748,153	53,943	98.04%	40,140	25.59%
	2019.04.01 23:47:00	1,427,587	64,763	95.46%	54,597	15.70%
	2019.04.05 23:38:41	2,792,371	171,358	93.86%	141,230	17.58%
	2019.04.30 22.22.58	1,147,088	321,121	72.01%	316,551	1.42%
	2019.05.24 09:23:05	2,655,007	44,265	98.33%	41,492	6.26%

contaminated by noise, and the trend shows a low-frequency change; thus, the change in the trend can be obtained through the MODWT. The results of each step are shown in Figure 6.

We used the MODWT algorithm in this study and the algorithm in [29] to conduct ground point extraction experiments on 14 pairs of ATL03 LAPs. The results for the 2019.04.05 23:38:41 gt1l track and 2019.06.02 20:50:35 gt3l track are

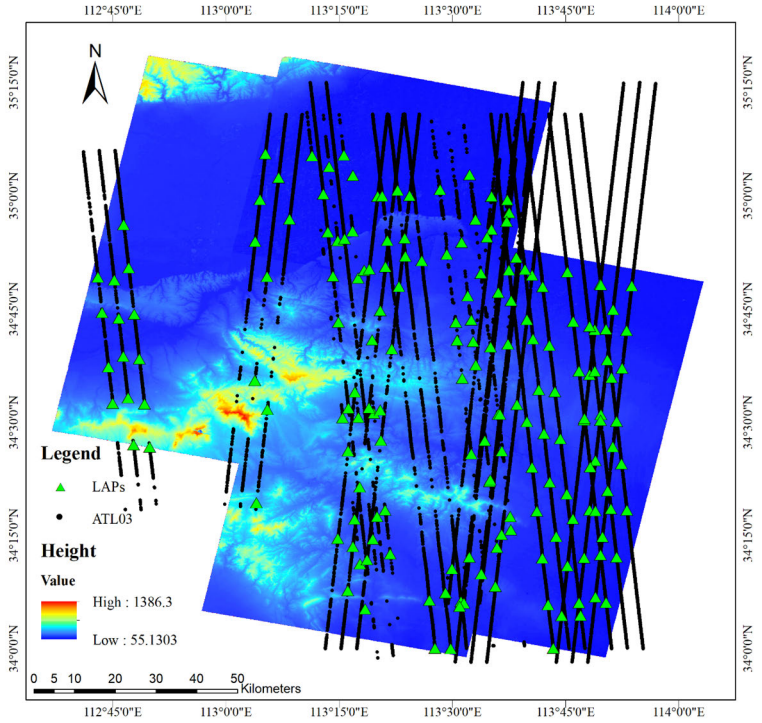

FIGURE 8. Selected LAPs distribution.

shown in Figure 7. The error statistics of the two algorithms are shown in Table 1.

The MODWT reconstruction removed most of the noise photons located at the surface and around the canopy, indicating that the use of MODWT reconstruction can extract ground points effectively without evaluation parameters to ensure the reliability of subsequent control point selection. Especially in mountainous areas, compared with the algorithm in [29], more ground points can be extracted by the MODWT reconstruction on steep slopes. After the ground points were extracted, the DEM was used for slope selection. The selection results of 14 pairs of ATL03 LAPs are shown in Table 2, and only the strong beam was selected. Night data showed a higher denoising rejection rate than day data, which indicated that night data had a high signal-to-noise ratio, so that the denoising effect was more significant.

After the reliable LAPs were filtered, the remaining points were more reliable as control points. The final LAPs distribution obtained after selection at 0.1° intervals within the track is shown in Figure 8, with a total of 180 points.

B. BLOCK ADJUSTMENT TEST OF LAPs AND SATELLITE STEREO IMAGES

To verify the effectiveness of adding the LAPs as a control condition to the adjustment and analyze the influence of the inconsistency of image-object points of the LAPs on the adjustment results, two adjustment experiments were carried out.

1) Block adjustment test of laps and zy3-02 stereo images
A total of 180 LAPs and ZY3-02 stereo images were selected for the block adjustment test. The experiments were designed as follows.

- Plan 1: block adjustment with 180 LAPs at the scheme considering the plane coordinate error of the LAPs.
- Plan 2: block adjustment with 180 LAPs at the scheme not considering the plane coordinate error of the LAPs.
- Plan 3: free network adjustment without LAPs.

In addition to the three types of adjustment experiment, another four types were designed, which both considered the plane coordinate error of the LAPs.

- Plan 4: thinning out 180 LAPs at 0.1° intervals, remaining 71 LAPs.
- Plan 5: thinning out 180 LAPs at 0.2° intervals, remaining 27 LAPs.
- Plan 6: eliminating LAPs located in mountain terrain from plan 4, remaining 173 LAPs.
- Plan 7: eliminating LAPs with a slope value of 2–6° from plan 10, remaining 154 LAPs.

The adjustment results of ZY3-02 were shown in Table 3 and Figure 9.

Without any GCPs (plan 3), the direct height, east, and north geolocation accuracy were 4.651, 13.679, and 11.144 m, respectively. When the LAPs were jointed to the block adjustment (plan 2), the height, east, and north accuracy increased noticeably by 57%, 48%, and 46%, respectively. When the plane coordinate error of the LAPs (plan 1) was

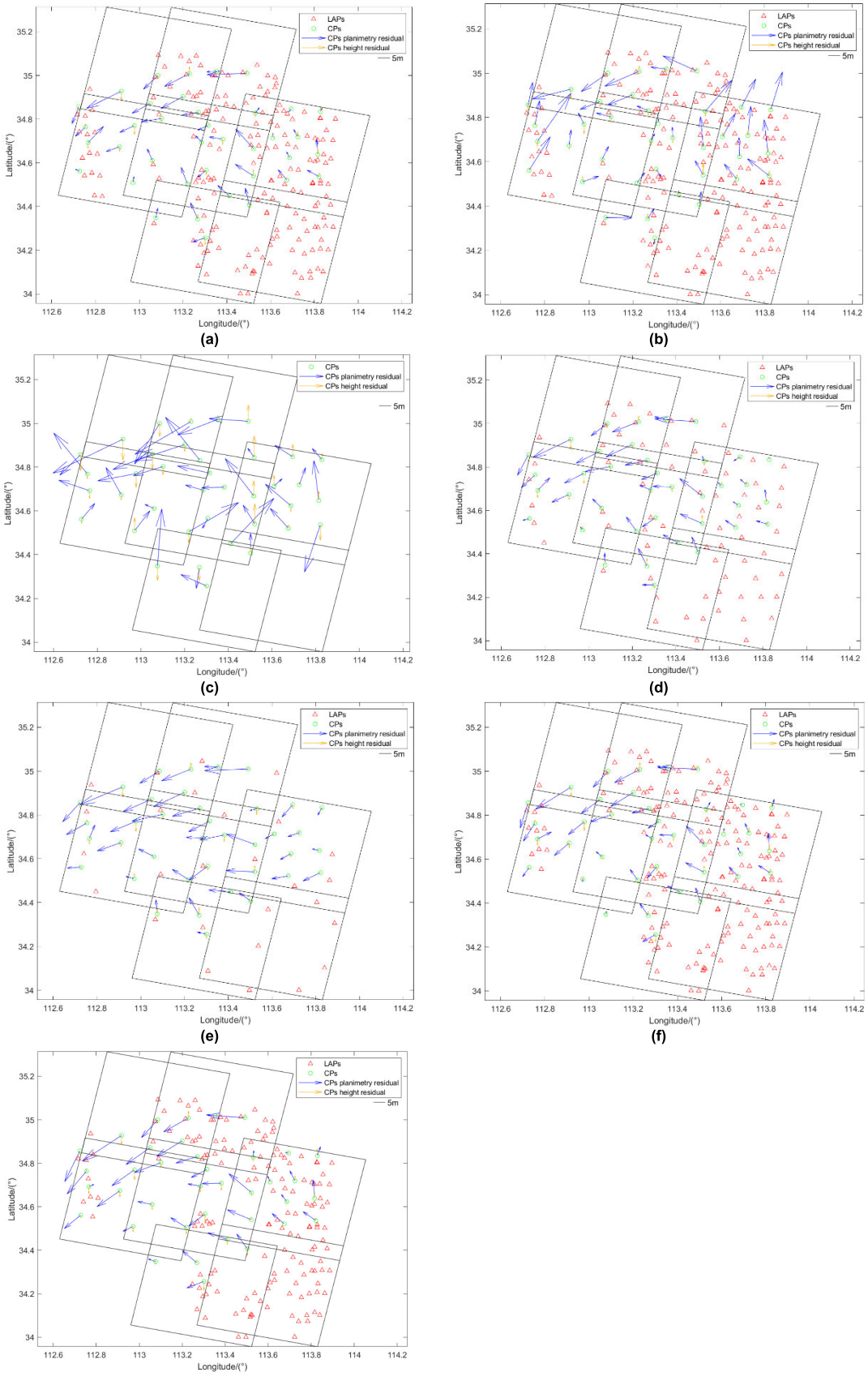

FIGURE 9. Comparison of the residuals of each ZY3-02 block adjustment plan. (a) Plan 1, (b) Plan 2, (c) Plan 3, (d) Plan 4, (e) Plan 5, (f) Plan 6, (G) PLAN 7.

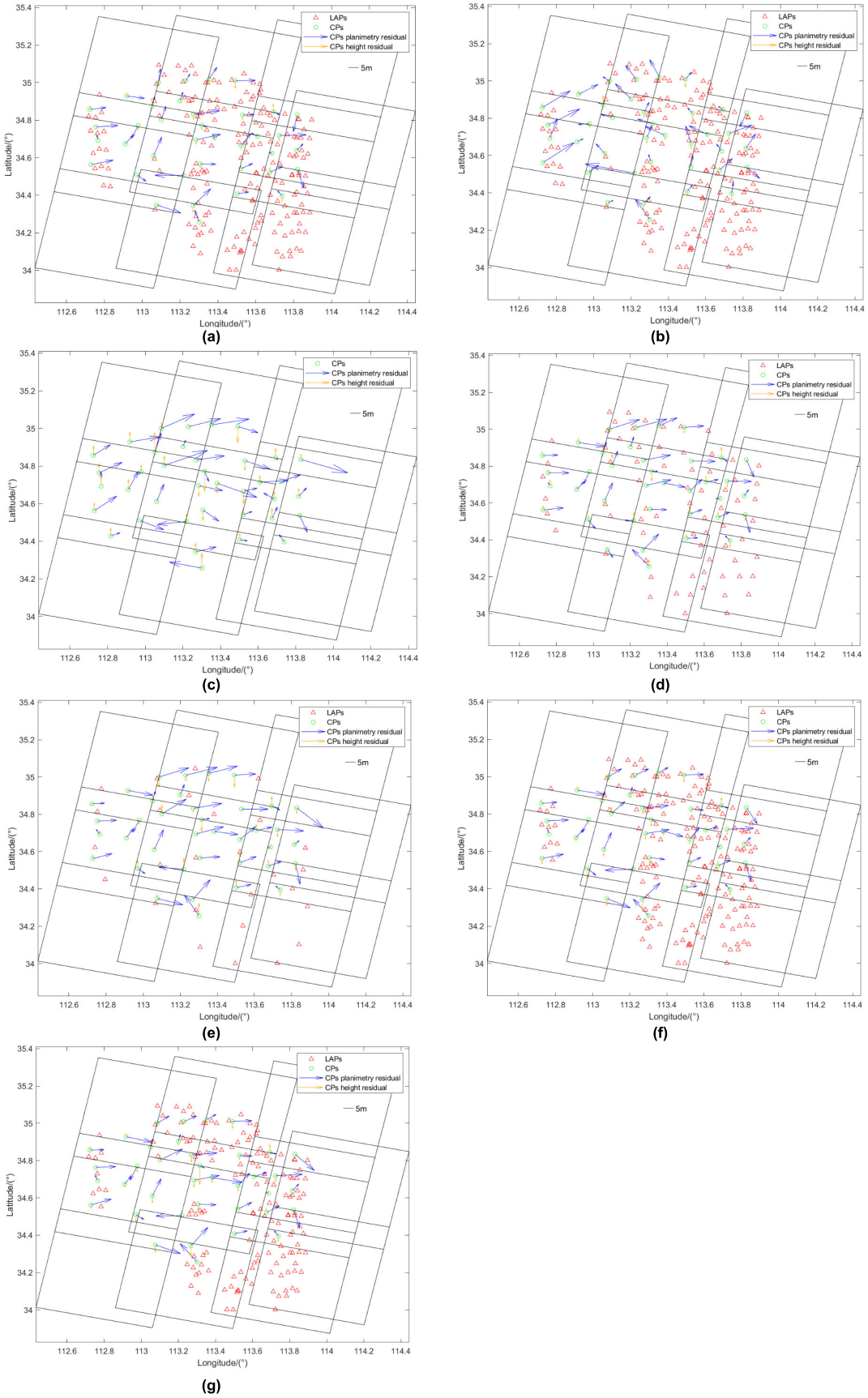

FIGURE 10. Comparison of the residuals of each mapping satellite-1 block adjustment plan. (a) Plan 1, (b) Plan 2, (c) Plan 3, (d) Plan 4, (e) Plan 5,(f) PLAN 6, (g) PLAN 7.

TABLE 3. Total adjustment results of ZY3-02 stereo images and LAPS.

Plan	Height accuracy/m			Planimetry accuracy/m					
	RMSE	Mean absolute difference	Maximum error	Planimetry RMSE	Planimetry maximum error	East RMSE	East maximum error	North RMSE	North maximum error
P1	1.798	1.529	-3.887	7.446	15.129	6.004	-16.671	4.404	8.509
P2	2.000	1.723	4.829	9.255	15.526	7.071	-16.029	5.971	12.713
P3	4.651	3.869	8.999	17.644	32.634	13.679	-29.375	11.144	-19.812
P4	1.876	1.519	-4.560	8.247	17.250	7.084	-17.217	4.222	-8.759
P5	1.822	1.503	-4.223	9.679	18.312	8.794	-18.299	4.043	-8.068
P6	1.799	1.546	-3.807	7.710	17.486	6.125	-16.550	4.682	-10.600
P7	2.136	1.840	-4.332	9.365	19.967	7.698	-16.780	5.334	-12.919

TABLE 4. Total adjustment results of mapping Satellite-1 stereo images and LAPs.

Plan	Height accuracy/m			Planimetry accuracy/m					
	RMSE	Mean absolute difference	Maximum error	Planimetry RMSE	Planimetry maximum error	East RMSE	East maximum error	North RMSE	North maximum error
P1	2.016	1.748	4.199	7.989	13.900	6.721	-13.900	4.320	-9.012
P2	2.270	1.929	4.574	9.439	17.550	7.632	15.675	5.553	10.003
P3	4.556	3.822	9.755	12.946	22.344	10.927	21.122	6.942	13.336
P4	2.595	2.062	5.758	9.009	16.047	7.883	15.485	4.361	-9.089
P5	3.192	2.656	6.136	10.411	16.169	9.288	15.680	4.704	-10.360
P6	2.548	2.170	-5.655	8.547	13.989	7.499	-13.978	4.101	-8.911
P7	2.865	2.327	-5.181	9.042	15.138	7.998	14.956	4.218	9.082

considered, the height, east, and north accuracy increased by 61%, 56%, and 60%, respectively.

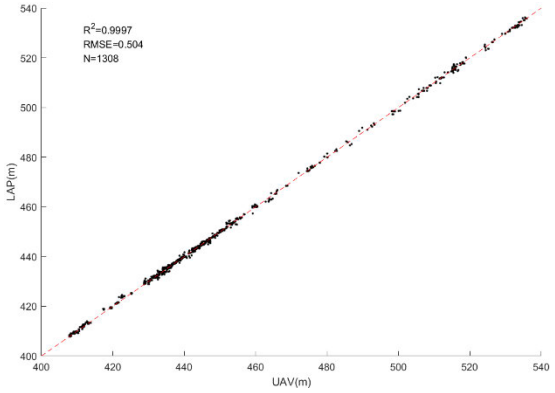

FIGURE 11. Scatterplot demonstrating the correlation between selected LAPs and UAV LiDAR.

TABLE 5. Statistical results for the height deviation between selected LAPs and UAV LiDAR.

Absolute value of height difference (Unit: m)	Number	Percentage
<0.2	725	55.4%
<0.4	995	76.1%
<0.6	1108	84.7%
<0.8	1157	88.5%
<1	1200	91.7%

The height and east accuracy decreased by 4% and 18%, respectively, but the north accuracy slightly increased by 4% between plans 1 and 4. The height accuracy was the same, the east accuracy decreased by 46%, and the north accuracy increased by 8% between plans 1 and 5.The height accuracy

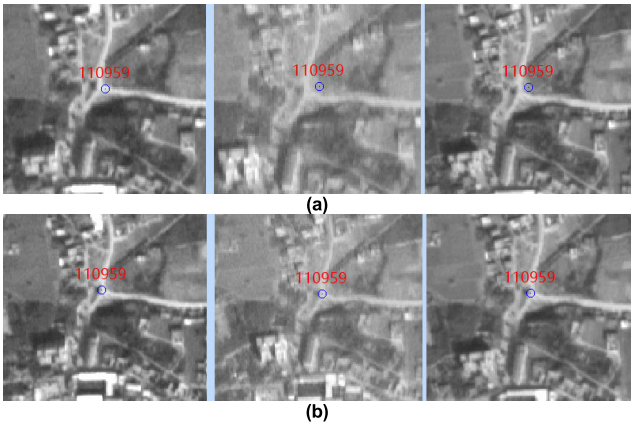

FIGURE 12. Detailed views for P57 overlaid on the stereo images, where the left image shows FWD, the center one shows BWD and the right shows NAD. (a) before adjustment, (b) after adjustment.

was basically unchanged, and the east and north accuracy decreased by 2% and 6%, respectively, between plans 1 and 6. The height, east, and north accuracy decreased by 19%, 28%, and 21%, respectively, between plans 1 and 7.

1) BLOCK ADJUSTMENT TEST OF LAPs AND MAPPING SATELLITE-1 STEREO IMAGES

To further verify the effectiveness of the joint adjustment method, 180 LAPs and Mapping Satellite-1 stereo images were selected for the block adjustment test. The adjustment results of Mapping Satellite-1 were presented in Table 4 and Figure 10.

The Mapping Satellite-1 satellite stereo image adjustment test demonstrated that the joint adjustment method of LAPs and satellite stereo images can significantly improve the adjustment accuracy. Considering the plane coordinate error

TABLE 6. Statistical results for CPs image point error.

Absolute value of image point difference (Unit: pixels)	Before block adjustment		After block adjustment	
	dL	dB	dL	dB
P113,34.6	2.7	11.4	2.3	3.4
P113.1,35	14.4	19.8	3.7	4.0
P113.3,34.3	2.8	4.5	2.0	2.5
P113.3,34.6	5.7	3.4	3.3	2.6
P113.4,35	3.2	3.7	3.2	3.1
P113.6,34.3	7.8	3.0	3.2	2.2
P113.7,34.6	4.2	5.1	2.4	2.1

TABLE 7. Statistical results for LAPs image point error.

Relative value of image point difference (Unit: pixels)	Before block adjustment	
	dL	dB
P113,34.6	2.1	1.8
P113.1,35	4.9	5.5
P113.3,34.3	3.1	2.0
P113.3,34.6	3.0	2.8
P113.4,35	3.1	4.4
P113.6,34.3	2.5	3.3
P113.7,34.6	2.2	2.1

of the LAPs, the joint adjustment scheme proposed in this study had the highest accuracy, and the height, east, and north accuracy increased by 56%, 38%p, and 37%, respectively. This was consistent with the conclusion of the ZY3-02 stereo image joint adjustment experiment.

The height and east accuracy decreased by 29% and 17%, respectively, but the north accuracy was basically the same between plans 1 and 4. The height, east, and north accuracy decreased by 58%, 38%, and 9%, respectively, between plans 1 and 5.The height and east accuracy decreased by 26% and 11%, respectively, and the north accuracy increased by 5% between plans 1 and 6. The height and east accuracy reduced by 42% and 19%, respectively, and the north accuracy was basically the same between plans 1 and 7.

V. DISCUSSION

A. ACCURACY EVALUATION OF SELECTED LAPs

To evaluate the height accuracy of selected LAPs, the 20181226163114 gt1r track was passed through the UAV LiDAR area. The selected LAPs with highly accurate UAV LiDAR data showed a strong correlation (Figure 11). A total of 1308 selected LAPs were analyzed in this area. The coefficient of determination (R^2) reached 0.9997, while the RMSE was 0.504 m, and the minimum and maximum values of the absolute height difference were 0.001 and 1.978 m, respectively. The height deviation distributions are listed in Table 4.

According to the statistical results for height accuracy, more than half of the points had a height difference of less than 0.2 m and could be used as control points for satellite stereo image block adjustment through reliable LAPs selection.

B. DISCREPANCIES IMPROVEMENT BETWEEN THREE-VIEW IMAGES

The image point differences were listed in Table 6 and Table 7, the left column represented ZY3-02 stereo images number, and the relative value of image point difference after block adjustment were both 0. The exact location of CPs was known, so the absolute image point difference of CPs in triple images was calculated. While the relative image point difference of LAPs in BWD and FWD images was calculated, using the NAD image as reference.

Taking P57 overlaid on the NAD, BWD, FWD images, the image points were not the homologous points, as shown in Figure 12a. The main error sources were the RPC parameters.

The LAPs and satellite stereo image joint block adjustments can significantly improve the accuracy of the adjustment. By correcting the object-space coordinates by iteration, LAPs were closer to the actual position, improving the consistency of image-object points and the accuracy of the adjustment, as shown in Figure 12b.

C. NECESSITY OF LAPs IN MOUNTAINOUS AREAS

The analysis of the number of points in plans 6 and 7 showed that after the reliable LAPs selection, most LAPs were determined to be in flat areas, but mountainous and hilly areas could also retain points that met the selection criteria.

The overall accuracy of plans 6 and 7 was not as high as that of plan 1 because sparse or no control points in mountainous and hilly terrains reduced the control intensity in this area. Comparing plan 1 with plan 6 and plan 7, the height accuracy of P57, P63, P70 decreased sharply, which are in mountainous areas. Increasing LAPs in mountainous areas can further restrain local distortions of the block, which greatly improves the height accuracy.

Therefore, in actual production, to ensure the overall block accuracy requirements, LAPs located in mountainous and hilly terrains should be used after selection.

D. SUMMARY OF THE EXPERIMENTAL RESULTS

The experimental results can be summarized as follows

(1) Viewed as a control condition after selection, LAPs can significantly improve the overall accuracy of the stereo images. If plane coordinates with errors are considered, the overall adjustment accuracy can be further improved. Owing to the lack of LAPs in the middle left area of the image, the plane accuracy in this area was poor. Because the plane coordinates of LAPs were not sufficiently accurate, their control range was relatively limited.

(2) For the same LAP overlaid on the NAD, BWD, and FWD images, the image points on three-view images were not the homologous points, which was mainly caused by the errors of RPC parameters. The proposed block adjustment method corrected the orientation parameters and eliminated discrepancies between three-view images.

(3) In mountainous areas, the reduction in LAPs will cause a significant decrease in accuracy. Because height changes rapidly in mountain areas, a small offset of the plane coordinates will cause a large change in the height error. Therefore, when performing joint adjustment processing on a satellite stereo image that contains a mountainous area, it is necessary to deploy LAPs in mountainous areas. The overall adjustment accuracy from plan 1 was the best, which also reflects that the LAPs selection method proposed in this study can be applied to mountainous areas.

VI. CONCLUSION

The ICESat-2/ATLAS showed satisfactory detection performance as the first laser altimeter satellite with photon-counting LiDAR. The results suggest that LAPs can be used as control points after selection. A surface point cloud extraction algorithm based on MODWT was proposed to extract ground information accurately without evaluation parameters. Subsequently, the influence of terrain factors was effectively reduced through slope selection. To solve the problem of errors in LAP's plane coordinates, and no synchronized observation image, the selected ATLAS LAPs were used as control points with a plane coordinate error for joint adjustment. Without other GCPs, the height accuracy of ZY3-02 stereo images can be improved to less than 2.0 m only using ATLAS LAPs, which can satisfy the requirements of 1:50,000 scale mapping. Moreover, the height accuracy of Mapping Satellite-1 stereo images can be improved to 2.016m, which proved the versatility of the method.

The optimization strategy was adopted to alleviate the problem of inconsistency in LAPs, but it has not yet been fully solved. There is still a need to further improve the adjustment accuracy. The precise position prediction of the LAPs will be further studied in future work. Since higher-resolution stereo images can achieve higher accuracy under similar conditions, high-resolution satellite stereo imagery will also be validated in future work.

ACKNOWLEDGMENT

The authors would like to thank the data distribution agencies for providing data: (1) ZY3-02 data were obtained from Satellite Surveying and Mapping Application Center, National Administration of Surveying Mapping and Geo-information. (2) ICESat-2 data were obtained from the ICESat-2 Project Science Office.

REFERENCES

[1] M. R. Rosiek, R. L. Kirk, B. A. Archinal, E. Howington-Kraus, T. Hare, D. Galuszka, and B. Redding, "Utility of viking orbiter images and products for Mars mapping," *Photogramm. Eng. Remote Sens.*, vol. 71, no. 10, pp. 1187–1195, Oct. 2005, doi: 10.14358/PERS.71.10.1187.

[2] J.-S. Yoon and J. Shan, "Combined adjustment of MOC stereo imagery and MOLA altimetry data," *Photogramm. Eng. Remote Sens.*, vol. 71, no. 10, pp. 1179–1186, Oct. 2005, doi: 10.14358/PERS.71.10.1179.

[3] K. Di, W. Hu, Y. Liu, and M. Peng, "Co-registration of Chang'E-1 stereo images and laser altimeter data with crossover adjustment and image sensor model refinement," *Adv. Space Res.*, vol. 50, no. 12, pp. 1615–1628, Dec. 2012, doi: 10.1016/j.asr.2012.06.037.

[4] Y. He, S. Wu, and X. S, "Block adjustment of Chang E-1 CCD images based on RFM," *Sci. Surv.*, vol. 38, no. 6, pp. 5–6, 2013, doi: 10.16251/j.cnki.1009-2307.2013.06.034.

[5] H. Duong, R. Lindenbergh, N. Pfeifer, and G. Vosselman, "ICESat full-waveform altimetry compared to airborne laser scanning altimetry over The Netherlands," *IEEE Trans. Geosci. Remote Sens.*, vol. 47, no. 10, pp. 3365–3378, Oct. 2009, doi: 10.1109/TGRS.2009.2021468.

[6] X. Wang, X. Cheng, Z. Li, H. Huang, Z. Niu, X. Li, and P. Gong, "Lake water footprint identification from time-series ICESat/GLAS data," *IEEE Geosci. Remote Sens. Lett.*, vol. 9, no. 3, pp. 333–337, May 2017, doi: 10.1109/LGRS.2011.2167495.

[7] B. Li, H. Xie, X. Tong, Z. Zhang, and S. Liu, "Extracting satellite laser altimetry footprints with the required accuracy by random forest," *IEEE Geosci. Remote Sens. Lett.*, vol. 18, no. 8, pp. 1–5, Aug. 2020, doi: 10.1109/LGRS.2020.2999201.

[8] G. Li, X. Tang, X. Gao, and Y. Wang, "ZY-3 block adjustment supported by GLAS laser altimetry data," *Photogramm. Rec.*, vol. 31, no. 153, pp. 88–107, 2016, doi: 10.1111/phor.12138.

[9] G. Li, X. Tang, X. Gao, C. Zhang, and T. Li, "Improve the ZY-3 height accuracy using ICESat/GLAS laser altimeter data," *ISPRS Int. Arch. Photogramm., Remote Sens. Spatial Inf. Sci.*, vol. 41, pp. 37–42, Jun. 2016, doi: 10.5194/isprsarchives-XLI-B1-37-2016.

[10] G. Li, X. Tang, X. Gao, X. Wang, W. Fan, J. Chen, and F. Mo, "Integration of ZY3-02 satellite laser altimetry data and stereo images for high-accuracy mapping," *Photogramm. Eng. Remote Sens.*, vol. 84, no. 9, pp. 569–578, Sep. 2018, doi: 10.14358/PERS.84.9.569.

[11] J. Wang, Y. Zhang, Z. Zhang, X. Li, P. Tao, and M. Xiao, "ICESat laser points assisted block adjustment for mapping satellite-1 stereo imagery," *Acta Geodaetica Cartographica Sinica*, vol. 47, no. 3, pp. 359–369, 2018, doi: 10.11947/j.AGCS.2018.20170425.

[12] N. Cao, P. Zhou, X. Wang, X. Tang, and G. Li, "Refined processing of laser altimeter data-aided satellite geometry model," *J. Remote Sens.*, vol. 22, no. 4, pp. 599–610, 2018, doi: 10.11834/jrs.20187252.

[13] A. J. Martino, T. A. Neumann, N. T. Kurtz, and D. McLennan, "ICESat-2 mission overview and early performance," *Proc. SPIE*, vol. 11151, Oct. 2019, Art. no. 111510C, doi: 10.1117/12.2534938.

[14] W. Becker, *Advanced Time-Correlated Single Photon Counting Techniques*. Berlin, Germany: Springer, 2005.

[15] M. D. Eisaman, J. Fan, A. Migdall, and S. V. Polyakov, "Invited review article: Single-photon sources and detectors," *Rev. Sci. Instrum.*, vol. 82, no. 7, Jul. 2011, Art. no. 071101, doi: 10.1063/1.3610677.

[16] T. Markus, T. Neumann, A. Martino, W. Abdalati, K. Brunt, B. Csatho, S. Farrell, H. Fricker, A. Gardner, D. Harding, and M. Jasinski, "The ice, cloud, and land elevation satellite-2 (ICESat-2): Science requirements, concept, and implementation," *Remote Sens. Environ.*, vol. 190, pp. 260–273, Mar. 2017, doi: 10.1016/j.rse.2016.12.029.

[17] C. E. Parrish, L. A. Magruder, A. L. Neuenschwander, N. Forfinski-Sarkozi, M. Alonzo, and M. Jasinski, "Validation of ICESat-2 ATLAS bathymetry and analysis of ATLAS's bathymetric mapping performance," *Remote Sens.*, vol. 11, no. 14, p. 1634, Jul. 2019, doi: 10.3390/rs11141634.

[18] A. L. Neuenschwander and L. A. Magruder, "Canopy and terrain height retrievals with ICESat-2: A first look," *Remote Sens.*, vol. 11, no. 14, p. 1721, Jul. 2019, doi: 10.3390/rs11141721.

[19] M. Wang, Y. Wei, B. Yang, and X. Zhou, "Extraction and analysis of global elevation control points from ICESat/2/ATLAS data," *Inf. Sci. Wuhan Univ.*, vol. 46, no. 2, pp. 184–192, 2021, doi: 10.13203/j.whugis20200531.

[20] A. Neuenschwander and K. Pitts, "The ATL08 land and vegetation product for the ICESat-2 mission," *Remote Sens. Environ.*, vol. 221, pp. 247–259, Feb. 2019, doi: 10.1016/j.rse.2018.11.005.

[21] T. A. Neumann, A. J. Martino, T. Markus, S. Bae, M. R. Bock, A. C. Brenner, K. M. Brunt, J. Cavanaugh, S. T. Fernandes, D. W. Hancock, and K. Harbeck, "The ice, cloud, and land elevation satellite–2 mission: A global geolocated photon product derived from the advanced topographic laser altimeter system," *Remote Sens. Environ.*, vol. 233, Nov. 2019, Art. no. 111325, doi: 10.1016/j.rse.2019.111325.

[22] X. Tang, H. Wang, and X. Zhu, "Technology and appilcations of surveying and mapping for ZY-3 satellites," *Acta Geodaetica Cartographica Sinica*, vol. 46, no. 10, pp. 1482–1491, 2017, doi: 10.11947/j.AGCS.2017.20170251.

[23] R. Wang, J. Wang, and X. Hu, "Preliminary location accuracy assessments of 3rd satellite of TH-1," *Acta Geodaetica Cartographica Sinica*, vol. 45, no. 10, pp. 1135–1139, 2016, doi: 10.11947/j.AGCS.2016.20160373.

[24] A. G. Hafez, E. Ghamry, H. Yayama, and K. Yumoto, "A wavelet spectral analysis technique for automatic detection of geomagnetic sudden commencements," *IEEE Trans. Geosci. Remote Sens.*, vol. 50, no. 11, pp. 4503–4512, Nov. 2012, doi: 10.1109/TGRS.2012.2192279.
[25] D. B. Percival and H. O. Mofjeld, "Analysis of subtidal coastal sea level fluctuations using wavelets," *J. Amer. Stat. Assoc.*, vol. 92, no. 439, pp. 868–880, 1997, doi: 10.1080/01621459.1997.10474042.
[26] S. Xing, G. Zhang, Q. Xu, X. Zhang, P. Li, K. Chen, and L. Wu, "Extraction algorithm based on optimized EMD with satellite laser altimetry data," *J. Geomat Sci. Technol.*, vol. 37, no. 3, pp. 294–300, 2020, doi: 10.3969/j.issn.1673-6338.2020.03.013.
[27] R. Lussana, F. Villa, A. D. Mora, D. Contini, A. Tosi, and F. Zappa, "Enhanced photon-counting time-of-flight 3D ranging," *Opt. Exp.*, vol. 23, no. 19, pp. 24962–24973, 2015, doi: 10.1364/OE.23.024962.
[28] L. L. Narine, S. Popescu, A. Neuenschwander, T. Zhou, S. Srinivasan, and K. Harbeck, "Estimating aboveground biomass and forest canopy cover with simulated ICESat-2 data," *Remote Sens. Environ.*, vol. 224, pp. 1–11, Apr. 2019, doi: 10.1016/j.rse.2019.01.037.
[29] Y. Xing, J. Huang, A. Gruen, and L. Qin, "Assessing the performance of ICESat-2/ATLAS multi-channel photon data for estimating ground topography in forested terrain," *Remote Sens.*, vol. 12, no. 13, p. 2084, 2020, doi: 10.3390/rs12132084.
[30] M. S. Moussavi, W. Abdalati, T. Scambos, and A. Neuenschwander, "Applicability of an automatic surface detection approach to micro-pulse photon-counting lidar altimetry data: Implications for canopy height retrieval from future ICESat-2 data," *Int. J. Remote Sens.*, vol. 35, no. 13, pp. 5263–5279, Jul. 2014, doi: 10.1080/01431161.2014.939780.
[31] Z. Li, Y. Deng, G. Zhang, and X. Yang, "Determination of best grading of wavelet transform in deformation measurement data filtering," *Inf. Sci. Wuhan Univ.*, vol. 36, no. 3, pp. 285–288, 2011, doi: 10.13203/j.whugis2011.03.006.
[32] C. Ren, L. Sha, and X. Lu, "An adaptive wavelet threshold de-noising for deformation analysis," *Inf. Sci. Wuhan Univ.*, vol. 37, no. 7, pp. 873–875, 2012, doi: 10.13203/j.whugis2012.07.021.
[33] A. Neuenschwander, K. Pitts, B. Jelley, J. Robbins, B. Klotz, S. Popescu, R. Nelson, D. Harding, D. Pederson, and R. Sheridan. (Apr. 15, 2020). *ICESat-2 Project ATBD for Land-Vegetation Along-Track Products*. ATL08. [Online]. Available: https://icesat-2.gsfc.nasa.gov/science/data-products
[34] C. V. Tao and Y. Hu, "A comprehensive study of the rational function model for photogrammetric processing," *Photogramm. Eng. Remote Sens.*, vol. 67, no. 12, pp. 1347–1358, 2001.
[35] X. Tong, S. Liu, and Q. Weng, "Bias-corrected rational polynomial coefficients for high accuracy geo-positioning of QuickBird stereo imagery," *ISPRS J. Photogramm. Remote Sens.*, vol. 65, no. 2, pp. 218–226, Mar. 2010, doi: 10.1016/j.isprsjprs.2009.12.004.

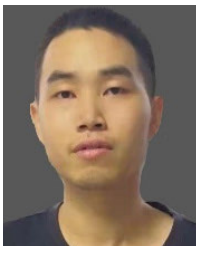

XINLEI ZHANG received the B.S. degrees in photogrammetry and remote sensing from the Institute of Geospatial Information, Information Engineering University, Zhengzhou, China, in 2017, where he is currently pursuing the Ph.D. degree. His research interests include noise filtering and block adjustment of spaceborne laser altimetry technology.

SHUAI XING received the B.S., M.S., and Ph.D. degrees in photogrammetry and remote sensing from the Institute of Geospatial Information, Information Engineering University, Zhengzhou, China, in 2001, 2004, and 2008, respectively. He is currently an Associate Professor and a Doctoral Supervisor with the Information Engineering University. His research interests include digital photogrammetry, LiDAR data acquisition and analysis, ocean remote sensing, and remote sensing data acquisition and analysis.

QING XU received the B.S., M.S., and Ph.D. degrees in photogrammetry and remote sensing from the Institute of Geospatial Information, Information Engineering University, Zhengzhou, China, in 1985, 1990, and 1995, respectively. He is currently a Professor and a Doctoral Supervisor with the Information Engineering University. His research interests include remote sensing and digital photogrammetry.

GUOPING ZHANG received the B.S. degrees in photogrammetry and remote sensing from the Institute of Geospatial Information, Information Engineering University, Zhengzhou, China, in 2019, where he is currently pursuing the M.S. degree. His research interest includes noise filtering of spaceborne laser altimetry technology.

PENGCHENG LI received the B.S., M.S., and Ph.D. degrees in photogrammetry and remote sensing from the Institute of Geospatial Information, Information Engineering University, Zhengzhou, China, in 2009, 2012, and 2015, respectively. He is a Lecturer with the Information Engineering University. His research interests include digital photogrammetry, LiDAR data acquisition and analysis, and remote sensing data acquisition and analysis.

KUN CHEN received the B.S. degrees in photogrammetry and remote sensing from the Institute of Geospatial Information, Information Engineering University, Zhengzhou, China, in 2019, where he is currently pursuing the M.S. degree. His research interest includes point cloud intelligent processing.